Presented at the 31st European PV Solar Energy Conference and Exhibition, 14-18 September 2015, Hamburg, Germany

DEVELOPMENT, CHARACTERIZATION AND MODELLING OF DOPING PROFILE, CONTACT RESISTANCE, AND METAL SPIKING IN DIFFUSED AND SCREEN-PRINTED BORON EMITTERS

Nico Wöhrle, Elmar Lohmüller, Sabrina Werner, Johannes Greulich
Fraunhofer Institute for Solar Energy Systems ISE, Heidenhofstraße 2, 79110 Freiburg, Germany
Telephone: +49 761 4588 5964, fax: +49 761 4588 7621, e-mail: nico.woehrle@ise.fraunhofer.de

ABSTRACT: Opposed to phosphorus n^+-emitters on p-type silicon solar cells, p^+-emitters on n-type silicon solar cells show altered properties with respect to e.g. dopant diffusion, electrical contacting, and metal induced recombination. This work tries to paint a consistent picture whose results base on deep-penetrating metal spikes (often also referred to as crystallites) formed below Ag-Al screen printing pastes during the contact firing process. By optimizing BBr_3 diffusion processes, emitter dark saturation current densities of as low as 30 fA/cm² on alkaline textured and passivated surface are obtained. For considering the interplay between boron doping profile and spike depth regarding the specific contact resistance ρ_C, BBr_3 diffusion processes are adapted yielding profiles with similar surface concentration but different junction depth. Apart from the maximum boron concentration, the junction depth of the doping profiles impacts ρ_C obtained for two examined Ag-Al pastes: deeper junctions lead to lower ρ_C. This finding is confirmed by an analytical model taking metal spikes with penetration depths of several 100 nm into account. The known issue of increased recombination below the Ag-Al metallization is addressed by a new simulation approach, which models the actual geometric shape of metal spikes in a three-dimensional (3D) simulation utilizing the quasi-steady-state photoconductance (QSSPC) technique. With these 3D QSSPC simulations, we discuss the impact of metal spiking in boron emitters in relation to depth and surface coverage of the spikes, and discuss the scenario which leads to dark saturation current densities of metallized boron emitters in the range of several 1000 fA/cm².
Keywords: boron-doped emitter; profile depth; dark saturation current density; contact resistance; metallization; spiking; crystallites; simulation; QSSPC; Sentaurus Device

1 INTRODUCTION

The performance of boron doped p^+-emitters is a major concern in the development of n-type silicon solar cells. Covering three aspects of boron emitters—process and electrical characterization, contact resistance, modelling of spiking—are targeted at conveying a deeper understanding of the functionality of boron emitters. It is meant to provide design rules for tailoring a boron emitter suitable for the solar cell concept of choice and guidance for its screen-printed and fired metallization.

The results of this work base on three recent publications addressing comprehensive development and characterization of boron emitter profiles for n-type silicon solar cells [1], specific contact resistance ρ_C [2], and simulation of spiking effects on the dark saturation current density beneath metal contacts $j_{0,met}$ [3]. The results of these three thorough investigations complement each other regarding their contributions to understanding the contact formation on boron-doped emitters and offer the extraction of design rules for metal pastes, doping profiles, and firing process optimizations. The work at hand intents to unite these aspects in a condensed form and gives a compact but comprehensive overview over the results and their implications for n-type silicon solar cell technology.

We start by introducing an analytical model for calculation of ρ_C and the quasi-steady-state-photoconductance (QSSPC) simulation model for three-dimensional (3D) $j_{0,met}$ simulations with metal spikes. In Section 3, we present an optimization of boron diffusion processes utilizing boron tribromide (BBr_3). This results in a set of well characterized boron emitter doping profiles forming the starting point for the further performed examinations. Section 4 deals with the results concerning the correlation between ρ_C and junction depth d_{junc}, both experimentally as well as with analytical calculations. The 3D QSSPC simulations of $j_{0,met}$ considering metal spikes are performed in Section 5. In Section 6 we review the results and extract conclusions for successful contact interface management.

2 THEORY

2.1 Analytical model for calculation of specific contact resistances

To analytically calculate ρ_C, the procedure introduced in Refs. [4,5] for silver contacts on phosphorus-doped surfaces forms the starting point. The analytical model applied in these works considers the three current transport mechanisms between metal and highly-doped silicon, namely thermionic emission (TE) [6], thermionic field emission (TFE) [7], and field emission (FE) [7].

Of course, for using the analytical model for boron-doped surfaces, the dopant-type-dependent variables concerning the applied current transport mechanisms are adapted to the p-type boron doping, as e.g. Schottky barrier height $q\Phi_b$, effective tunneling mass m_t^*, and effective Richardson constant A^*. As the boron dopant concentration for the doping profiles under investigation is always lower than 10^{20} cm^{-3}, FE processes do not have to be taken into account [2]. Hence, the applied analytical model considers parallel connection of TE and TFE processes.

Furthermore, it is assumed that current transport occurs exclusively via metal spikes in direct contact with both the bulk of the Ag-Al contact and the boron-doped emitter. Therein, the depth-dependent progression of the boron doping profile is taken into account. For the calculations, the following assumptions/simplifications are made:

- The considered wafer surface is smooth and parallel to the (100) crystal plane of silicon, and
- the spikes are represented by fully-formed inverted pyramids with quadratic base grown into the boron-doped silicon surface with an angle of 54.7° [6] to the (100) plane.

The approach pursued allows for calculating ρ_C depending on e.g. doping profile $N(d)$, spike penetration depth d_{spike}, and spike coverage fraction A_{spike}. An in-depth description of the analytical model with all applied formulae and input parameters can be found in Ref. [2].

2.2 Determination of emitter dark saturation current densities of highly-doped and passivated surfaces

The emitter dark saturation current densities j_{0e} of alkaline textured samples with highly-doped and passivated surfaces are extracted from QSSPC [8] measurements utilizing the slope-method introduced by Kane and Swanson [9]. For data analysis, the latest evaluation procedure from Kimmerle *et al.* [10] is applied, for which j_{0e} is given by

$$j_{oe} = \frac{qW}{2} \frac{\mathrm{d}}{\mathrm{d}\Delta n} \frac{n_{i,eff}^2(\Delta n)}{\left(\tau_s - \frac{W^2}{D_{amb}\pi^2}\right)}, \qquad (1)$$

with elementary charge q, sample thickness W, effective intrinsic carrier density $n_{i,eff}$, excess carrier density in the base region Δn, ambipolar carrier diffusion constant D_{amb}, and surface carrier lifetime τ_s.

2.3 3D QSSPC simulation of dark saturation current density beneath metal contacts

We emulate the experimental technique of the injection-dependent charge carrier lifetime measurement with *Sentaurus Device* [11], which can be done, e.g., using the QSSPC measurement technique developed by Sinton *et al.* [12]. Therein, the j_{0e} is extracted according to Eq. (1). A 2D-cross-section of the 3D model's symmetry element through the spike tip plane is depicted in Fig. 1.

The symmetry element is symmetrical in built regarding front and rear side geometry and doping profiles. For this characterization method, the base region is also boron doped. A flash with exponential decay is applied illuminating this virtual sample. Here the simulation has a major advantage compared to the experiment, as the metal layer covering the surface can be defined optically transparent while still retaining the electrical features of a metal contact, especially recombination characteristics. $j_{0,met}$, which is equal to j_{0e} in this approach due to complete surface metallization, then is extracted according to Eq. (1).

Although the virtual sample is covered with a metal layer, QSSPC measurements/simulations are conducted without contacting the probe, meaning no current extraction through the contact occurs; so we expect the ρ_C to have little impact on the results. Although no pn-junction is present, which is possibly distorted by deep spikes, the observation window for the QSSPC simulation ends shortly above the pn-junction. Spikes deeper than that lower the excess carrier density to a degree, where no reasonable evaluation is possible anymore. We already touch the limits of the *Sentaurus Device* metal interface model by applying metal layers to an inhomogeneously doped silicon boundary, as it is the case for the spike flanks. A spike reaching from the surface as far as the lowly-doped base region would be too much of a speculation in terms of modeling and would not be covered by the implemented metal boundary models in *Sentaurus Device*.

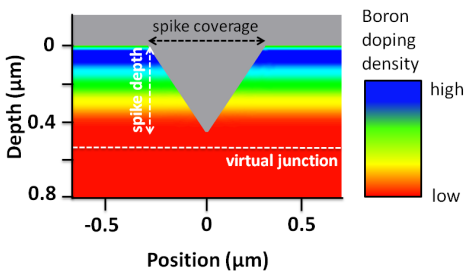

Fig. 1. Cross section through the spike tip plane. The virtual junction for an actual doping profile is indicated (the QSSPC model does not have a junction).

3 OPTIMIZED BBR_3 DIFFUSION PROCESSES

For a deeper understanding of the functionality of boron emitters regarding the correlation of ρ_C to the junction depth or the dependence of $j_{0,met}$ on the profile progression, tailoring of doping profiles needs to be possible. Profiles with the same maximum dopant concentration N_{max} but different depth or profiles with similar depth but different N_{max} are desirable. Several BBr_3 diffusion process variations have been performed to find such profiles. Now, one investigation is discussed in more detail, where only one process parameter has been stepwise adjusted.

The starting point in the generation of boron doping profiles is emitter profile Em A depicted in Fig. 2, a doping profile with a maximum dopant concentration $N_{max} = 9.1 \cdot 10^{19}$ cm^{-3} and an emitter sheet resistance $R_{sh} = 66$ Ω/sq. The doping profiles are determined by electrochemical capacitance voltage measurements (ECV). The BBr_3 diffusion process features a post-oxidation (PO) step right after the drive-in step which leads to the pronounced depletion at the wafer surface as the solubility of boron is higher in silicon oxide than in silicon [13].

The performed experiment aims at reducing the recombination activity of passivated and textured boron-doped surfaces by lowering N_{max}. One approach is to prolong the PO. Starting from process Em A, which features the standard PO, five variations with longer PO are investigated, while keeping the other parameters as for Em A. The resulting profiles are given in Fig. 2. With stepwise increasing PO from process Em A to process Em F, N_{max} decreases while the profiles become deeper. The reasons for this result are segregation of boron into the growing silicon oxide layer at the silicon interface, oxidation enhanced diffusion of boron, and longer diffusion times in general [13,14]. Further details on the conducted BBr_3 diffusion processes can be found in Ref. [1]. For Em F, this results in $N_{max} \approx 1.8 \cdot 10^{19}$ cm^{-3} and a depth $d \approx 850$ nm, yielding $R_{sh} = 104$ Ω/sq.

In Fig. 3, the j_{0e} for the diffusion processes with adapted PO are depicted. The respective open-circuit voltage limit $V_{OC,limit}$ is also specified. The j_{0e} is determined by QSSPC measurements on samples as shown in Fig. 3 using Eq. (1). The samples feature alkaline textured, highly doped surfaces that are passivated by a layer stack of Al_2O_3/SiN_x deposited by plasma enhanced chemical vapor deposition (PECVD).

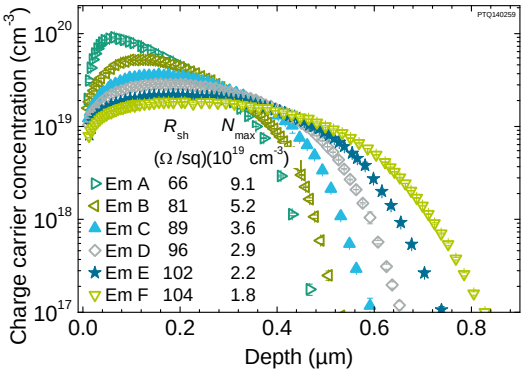

Fig. 2. Charge carrier concentration profiles determined by ECV measurements for different variations of the post-oxidation step within the BBr_3 diffusion process basing on Em A. The measurements are performed on alkaline saw-damage etched surfaces at the samples' center positions. The R_{sh} measured by means of inductive coupling at the ECV measurement spots as well as N_{max} are specified.

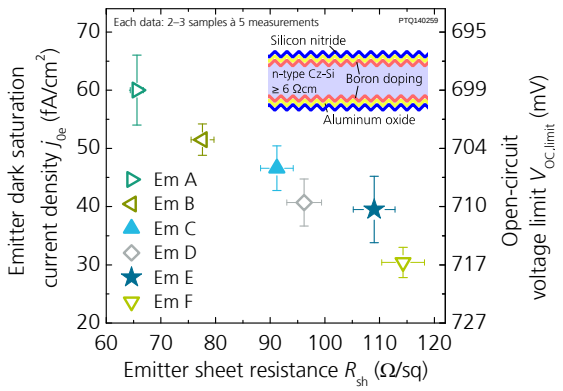

Fig. 3. Dark saturation current densities j_{0e} of alkaline textured and passivated (PECVD Al_2O_3/SiN_x) samples after firing in dependence of emitter sheet resistance R_{sh} measured by means of inductive coupling. The error bars represent the standard deviation of the measurement data reflecting the uniformity in j_{0e} and R_{sh} over the wafer surface for more than one wafer. The open-circuit voltage limit $V_{OC,limit}$ is calculated from j_{0e} by using the one-diode model with j_{SC} = 39 mA/cm² and temperature T = 25°C.

It is seen that linear correlation exists between R_{sh} and j_{0e}: the higher R_{sh}, the lower j_{0e}. The more the PO is extended, the lower the recombination at the surface and the lower the Auger recombination within the emitter volume, which results in lower j_{0e}. Thus, with varying the PO, j_{0e} is significantly reduced from j_{0e} = 60 fA/cm² for Em A to j_{0e} = 30 fA/cm² for Em F. This emitter allows for a $V_{OC,limit}$ = 717 mV, resulting in an increase of 18 mV in $V_{OC,limit}$ with respect to emitter Em A.

BBr_3 diffusion Em F is a very promising candidate for further developments and its implementation into n-type silicon solar cells. Besides a high $V_{OC,limit}$ = 717 mV, this process with reduced N_{max} is found to be electrically contactable by screen-printed and fired silver-aluminum contacts with a specific contact resistance ρ_C below 4 mΩcm². This ρ_C is on the same level with that for process Em A. Thus, the larger junction depth of Em F is beneficial for achieving a low ρ_C as will be shown in the following section. Further, a benefit for larger junction depth is also anticipated regarding less recombination underneath the metal contacts based on the findings of Section 5.

4 IMPACT OF JUNCTION DEPTH ON SPECIFIC CONTACT RESISTANCE

The impact of an increase in junction depth of the boron emitter on ρ_C is examined utilizing two commercially available Ag-Al screen printing pastes from different manufacturers, referred to as "Ag-Al1" and "AgAl2". For this purpose, three boron doping profiles with different junction depths but nearly equal curve progressions in the near-surface region are utilized, which are a result from the before mentioned investigations. The ρ_C are measured on alkaline textured and passivated surfaces after contact firing according to the transmission line model (TLM) [15,16].

4.1 Approach

Starting with Em A, two further boron doping profiles – Em G and Em H – with similar N_{max} but deeper junctions are considered; see Fig. 4. The ρ_C are determined on the front side of final n-type Cz-Si solar cell

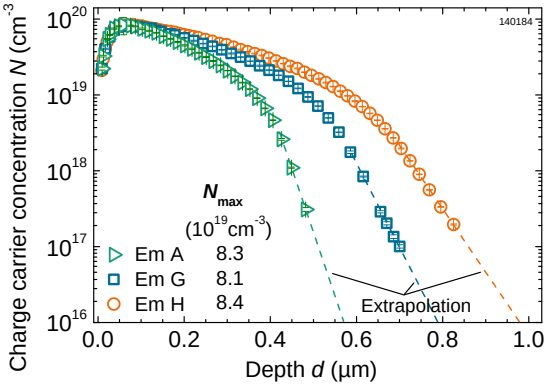

Fig. 4. Boron doping profiles $N(d)$ determined by ECV measurements at the center of alkaline textured wafers for the specified BBr_3 diffusion processes. The maximum dopant concentrations N_{max} are specified.

structures with Al_2O_3 and SiN_x passivation layer both applied by PECVD. The fabrication process of the samples using sequential diffusion processes is discussed in more detail in Ref. [2]. After contact firing in an industrial conveyor belt furnace (peak wafer temperature ≈ 720°C for < 1 s), all samples are cut into 10 mm-wide strips and ρ_C is determined by the TLM method. The finger widths are ≈ 80 µm for both Ag-Al pastes. For each boron doping with each Ag-Al paste, two wafers are examined. The TLM measurements are performed at six different positions per wafer in the wafer center where the diffusion process formed a very homogenous boron doping.

4.2 Specific contact resistance

Fig. 5 shows the measured ρ_C, which are overall very low with $\rho_C \leq 5$ mΩcm². A clear trend is visible for both Ag-Al pastes and the three boron doping profiles; lower ρ_C is measured for increasing junction depth d_{junc}: ρ_C for paste Ag-Al1 decreases from ρ_C = (3.7 ± 0.8) mΩcm² for Em A (d_{junc} ≈ 570 nm) to ρ_C = (2.0 ± 0.4) mΩcm² for Em H (d_{junc} ≈ 980 nm). Paste Ag-Al2 shows consistently about half the ρ_C as paste Ag-Al1 for each doping profile with the same trend regarding the junction depths. This result demonstrates that the measured ρ_C is significantly affected by the levels of doping concentration behind the dopant's peak (N_{max}), i.e. the profile's shape. Thus, N_{max}

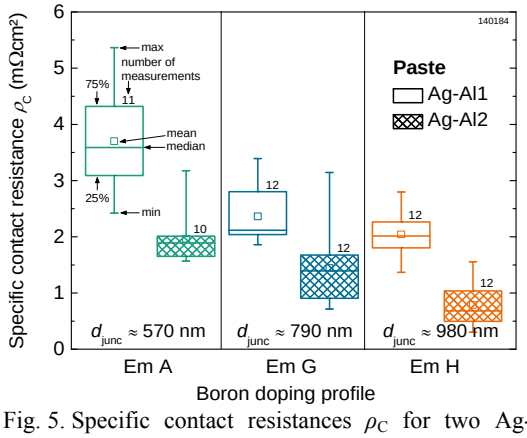

Fig. 5. Specific contact resistances ρ_C for two Ag-Al pastes obtained by TLM measurements on alkaline textured and boron-doped surfaces after contact firing. The surfaces are coated with a layer stack of Al_2O_3 and SiN_x both applied by PECVD. The junction depths d_{junc} of the boron doping profiles are also stated. The meaning of the box plots is exemplary explained for the first data set.

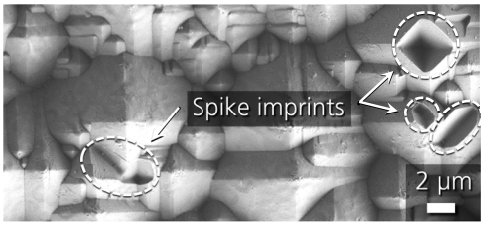

Fig. 6. SEM image of an alkaline textured Cz-Si surface with boron doping Em G after wet-chemical etching of paste Ag-Al2, the glass layer, the passivation layer stack, and the metal spikes after contact firing. Each imprint was occupied by a spike before wet-chemical etching.

is not the only parameter which determines the low resistance electrical contactability of boron-doped surfaces utilizing Ag-Al contacts. On the other hand, it is also clear that the Ag-Al paste itself has a major influence on the electrical contact formation.

4.3 Microstructure investigation of the contact interface

To investigate the silicon surface below the screen-printed and fired Ag-Al contacts, scanning electron microscopy (SEM) images are taken after wet-chemical etching of the TLM measurement strips. An exemplary SEM image is shown in Fig. 6. The marked spike imprints imply a former metal spike presence at these locations [17]. The crystallites were either in direct contact to the bulk metal or separated from it by an intermediate thin glass layer. Different sizes of crystallite imprints can be observed, also very large and thus deep imprints are apparent. This finding is in line with the findings from other authors [18–20]. The imprints are significantly larger in size than those observed for silver pastes on phosphorus-doped surfaces [17]. Further examinations reveal that the spikes penetrate some 100 nm up to several microns deep into the boron-doped emitter surfaces, and the spike coverage is found to be in the range of 1% [2].

4.3 Analytical model for calculating specific contact resistances

The analytical model, introduced in Section 2.1, allows for calculation of ρ_C dependent on e.g. doping profile $N(d)$, spike penetration depth d_{spike}, and spike coverage fraction A_{spike}. Refer to Ref. [2] for a detailed discussion of the performed calculations. Here, only a subset of the results is discussed. Fig. 7 depicts the relative changes

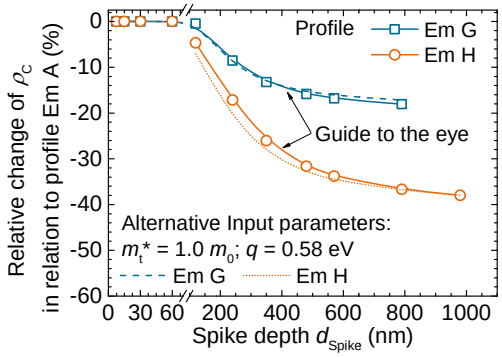

Fig. 7. Calculated relative changes in ρ_C for the profiles Em G and Em H in relation to ρ_C for profile Em A (used input parameters: see the text, other values for m_t^* and $q\phi_b$ are used as indicated). For profile Em A, $N(d)$ is set to 10^{16} cm^{-3} for larger depths than the junction depth in order to be able to calculate relative differences for $d_{spike} > d_{junc} = 570$ nm.

for the calculated ρ_C with varying d_{spike} in relation to the ρ_C obtained for boron profile Em A. The solid lines are calculated with an effective tunneling mass $m_t^* = 0.5\ m_0$ (m_0: electron mass), and a Schottky barrier height $q\Phi_b = 0.54$ eV. To demonstrate that the calculated relative ρ_C-differences are more or less independent of the used input parameters, the effective tunneling mass m_t^* and the Schottky barrier height $q\Phi_b$ are also varied (dashed/dotted lines). Since only the ratios of ρ_C are of interest for this comparison, the results are independent on A_{spike}. No difference in ρ_C is visible for $d_{spike} \leq 60$ nm. For $d_{spike} > 60$ nm, an impact on ρ_C due to the different doping profile progressions is evident: ρ_C decreases relative to profile Em A for the deeper profiles Em G and Em H in dependence of d_{spike}. The lowest ρ_C is obtained for profile Em H. The relative differences in ρ_C between (i) profile Em A and Em G of up to $\approx -20\%$ and (ii) profile Em A and Em H of up to $\approx -40\%$ are in the range of the experimentally determined differences; see Fig. 5. The most significant relative reduction in ρ_C results for $d_{spike} < 500$ nm. Although varying the input parameters leads to slight changes in the ρ_C-curves, the clear relative differences for profile Em G and Em H in comparison to profile Em A further remain. Hence, the simulation results clearly show that lower ρ_C results for doping profiles with deeper junctions. Finally, the process induced depletion region in the first 60 nm of the profile doesn't have an influence on ρ_C, if the spikes are deeper than these 60 nm. This is also considered in detail in Ref. [2].

5 3D QSSPC SIMULATION OF DARK SATURATION CURRENT DENSITY BENEATH METAL CONTACTS

5.1 Approach

The next topic of interest is the impact of the in Fig. 6 depicted spikes on $j_{0,met}$ of the emitter doping profiles. Here, too, we take Em A as a starting point. In addition, the emitter with the lowest j_{0e}, Em F, is taken into account; see Fig. 8. Two further variations of BBr_3 diffusion process parameters yield the two intermediate doping profiles Em I and Em J, which are also examined.

The emitter profiles Em A, Em F, Em I, and Em J are simulated with varied spike surface coverage A_{spike} and depth d_{spike}, as described in Section 2.3. The surface recombination velocity at the metal-silicon interface is set to $S_{met} = 10^7$ cm/s and $j_{0,met}$ is extracted.

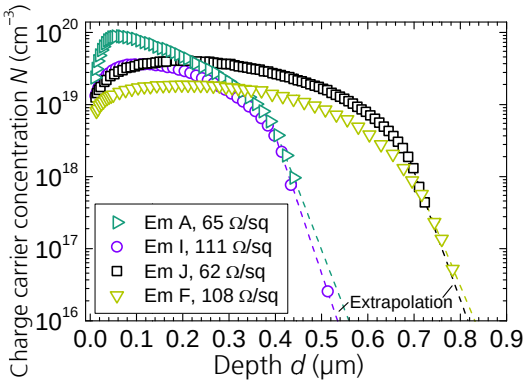

Fig. 8. Emitter doping profiles Em A, Em F, Em I, and Em J, which are chosen for the $j_{0,met}$ simulation, as they exhibit a partly crosswise variation in surface coverage and junction depth.

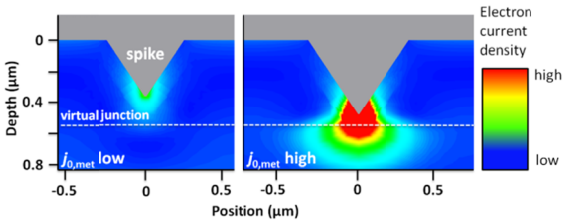

Fig. 9. 2D cross-section through the spike tip plane of the 3D element. The spike surface coverage in the 3D element is 20%. Shown is the electron current density increase close to the spike tip under illumination during the QSSPC flash. The figure intends to show the general mechanisms; therefore the exact figures are not of importance.

5.2 Simulation results for $j_{0,met}$

The general recombination mechanism occurring at spikes under illumination is visualized in Fig. 9: the spike tip, through to its exposed location in lower doped regions than the rest of the metallization, shows increased minority charge carrier recombination. If the tip gets closer towards the lowly-doped base region, more and more carriers are attracted due to the reduced impression of the shielding emitter region. This results in greatly increased $j_{0,met}$ levels.

The plots in Fig. 10 show the simulation results for $j_{0,met}$ obtained for the emitter profile Em A. The results for profiles Em F, Em I, and Em J feature comparable trends in $j_{0,met}$ (not shown). For all A_{spike}, $j_{0,met}$ stays almost constant at a low level up to a certain spike depth. This point is roughly 250 nm before reaching the virtual junction. Starting around this depth, $j_{0,met}$ increases rapidly. Em A shows a large $j_{0,met}$ increase from around 800 fA/cm² to over 4000 fA/cm² between d_{spike} = 0.2 µm and 0.5 µm for $A_{spike} \geq 10\%$. Nevertheless, for A_{spike} = 1%, we do only see a small increase from $j_{0,met}$ = 800 fA/cm² to 1000 fA/cm. The emitter profiles Em F, Em I and Em J yield comparable results, which are reviewed in Ref [3].

To have a reference for the $j_{0,met}$, measurements from processed samples were taken into account. The measurements are described in detail in Ref. [3]. The experimentally determined $j_{0,met}$ for Em A is plotted in Fig. 10 as a grey horizontal line.

Reviewing the experimental results, we see that the experimental $j_{0,met}$ can be met with the simulations assuming a $A_{spike} \geq 10\%$ in combination with deep spikes for

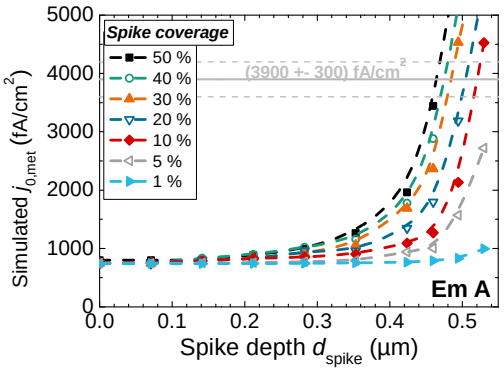

Fig. 10. 3D QSSPC simulation results for $j_{0,met}$ with varied spike coverage A_{spike} and spike penetration depth d_{spike} for Em A. The dashed curves are smoothed for better visibility of the trends. The grey horizontal line indicates the $j_{0,met}$ calculated with the help of the measured spiked samples.

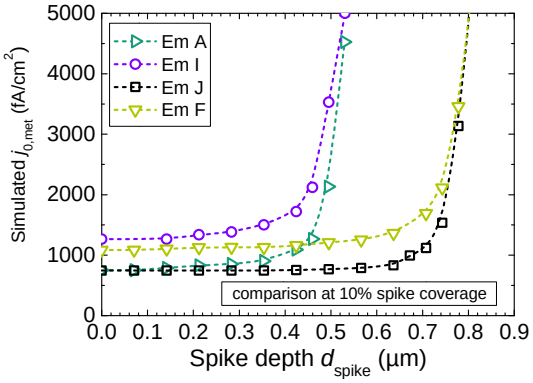

Fig. 11. Comparison of the $j_{0,met}$ curves for the four emitter profiles for 10% spike coverage.

the examined doping profile (and also for Em F, Em I, and Em J).

5.3 Discussion

Our simulations show that shallow spikes of any examined A_{spike} are not harmful to the emitter's $j_{0,met}$. Noticeable increase in $j_{0,met}$ starts at about d_{spike} = 2500 nm for $A_{spike} \geq 10\%$. If spikes approach the junction-depth, the spike tip reaches into doping levels low enough to give raise to pronounced carrier recombination. We define this as critical zone. Its limit depends on the doping profile shape, but a reasonable fixpoint could be set at 250 nm above the junction. A carrier density gradient towards the spike tip develops which leads to more and more carriers diffusing there. Fig. 9 demonstrates this for the electron current density. The closer a spike tip reaches towards the junction, the more this effect is pronounced, leading to the over-exponential $j_{0,met}$ curve, especially for A_{spike} above 10%.

To emphasize the impact of profile depth, Fig. 11 shows the 10% coverage $j_{0,met}$-curve for all four emitter profiles. Deeper emitter profiles tolerate deeper spikes, which conforms to our explanations of the observed effect. Also we see that irrespective from the $j_{0,met}$ at shallow spike depths of the doping profiles, the steep increase is comparable for the two shallow profiles or the two deep profiles. This means, deep spiking dominates $j_{0,met}$ to an extent, where the surface concentration of the doping profile almost loses its importance.

For every emitter we reach the $j_{0,met}$ calculated based on measurements for spike coverages of 10% and higher before the spike depth passes the pn-junction of a solar cell equipped with the respective doping profile. In no case, we can show the measured results inside our observation window (which does not reach up to the junction depth) for the experimentally observed coverage of 1%. This though was not necessary to show, as we know from imaging results (Fig. 6), that some spikes have a surface expansion which geometrically indicates a penetration into the base region. That leaves us with two inclusions: either the surface coverage of the examined samples is larger than 1%; a case we cannot exclude, since the coverage measurement was only performed at one probe and thus cannot be generalized. Or we have the case that – at coverage fractions of 1% and lower – spikes become only relevant if they penetrate through the junction. This conforms to our experimental results of a largely increased $j_{0,met}$, which influences V_{OC}. The effect on the fill factor *FF* due to shunting will not be discussed

here as the simulation physics do not suffice in terms of contact modeling here (see Section 2.3).

As a last point we would like to point out that 3D modelling is inevitable when simulating spikes. 2D spike models overestimate the $j_{0,met}$ increase heavily. This is explainable by geometrical considerations: 2D spikes, extrapolated to the third dimension, are effectively V-grooves and not inverted pyramids. Therefore their tip is effectively an edge, which increases the crucial recombination interface massively. Therefore, 2D models are not suitable for these simulated geometries.

6 CONCLUSION

Our starting point is the emitter profile "Em A" with high maximum doping concentration $N_{max} = 9.1 \cdot 10^{19}$ cm^{-3} and a dark saturation current density $j_{0e} = 60$ fA/cm².

The first stage of this work is a process variation for BBr_3 diffusion with prolonged post-oxidation leading to a cluster of emitter shapes with decreasing N_{max} and increasing junction depth d_{junc}. The emitter with the deepest junction (Em F) emerged as the one with the lowest $\boldsymbol{j_{0e} = 30}$ **fA/cm²** on alkaline textured and passivated surface in conjunction with $\boldsymbol{N_{max} = 1.8 \cdot 10^{19}}$ **cm^{-3}**, $\boldsymbol{d_{junc} = 0.85}$ **µm**, and a sheet resistance $\boldsymbol{R_{sh} = 115}$ **Ω/sq**.

The second stage sets the focus on the metallized emitter region. Even emitter Em F with the lowest N_{max} of the cluster of stage one could be electrically contacted with a specific contact resistance $\rho_C < 4$ mΩcm² using a commercially available silver-aluminum paste. Hereby, the question arised how the emitter profile shape in conjunction with metal spikes influences ρ_C. Two derivates of Em A with identical curve progression in the near-surface region but deeper junctions are experimentally realized, showing that the deeper profiles yield lower ρ_C. Analytical calculations, taking into account direct current conduction between metal spikes and the bulk contact, reveal also that the junction depth impacts ρ_C: the **deeper** the **junction**, the longer the metal spike's flanks experience higher doped regions which contributes to **lower** $\boldsymbol{\rho_C}$.

In the third stage, the impact of metal spiking on the emitter dark saturation current density $j_{0,met}$ beneath the metallized area is investigated by 3D *Sentaurus Device* QSSPC simulations. For that, we again employed the doping profile Em A, our champion emitter Em F (see first stage) and two intermediate profiles (Em I and Em J). As a result we see that the **emitters seem quite unaffected by shallow spiking** regarding recombination currents. $j_{0,met}$ only increases slightly as spikes progress towards greater depths within the emitter profile. However, each emitter profile has a critical zone above the junction line. If a spike's tip reaches into this zone, $j_{0,met}$ experiences an over-exponential increase originating from the spike tip, quickly leading to $j_{0,met}$ of several thousands of fA/cm². This **critical zone** depends on the emitter profile shape, but could roughly be set to **250 nm above the junction line**. Resulting from this recognition, deeper emitter profiles are much more robust against deep spiking.

Finally we can state that the formation of metal spikes on metallized boron emitters is a desirable feature regarding contact formation, if their depths can be controlled. Therefore metal pastes and firing processes should be optimized such that shallow spikes in sufficient number are formed. Further, we recommend deep boron emitter profiles for n-type solar cells which allow for low ρ_C and are more robust against deep spiking.

ACKNOWLEDGEMENTS

This work was funded by the German Federal Ministry for Economic Affairs and Energy within the research project "THESSO" under contract 0325491.

N. Wöhrle gratefully acknowledges the scholarship of the German Federal Environmental Foundation ("Deutsche Bundesstiftung Umwelt", DBU).

REFERENCES

[1] S. Werner, E. Lohmüller, U. Belledin, A. Vlooswijk, R. Naber, S. Mack, and A. Wolf, "Optimization of BBr3 diffusion processes for n-type silicon solar cells," in *31st EUPVSEC Hamburg*, 2015.

[2] E. Lohmüller, S. Werner, R. Hoenig, J. Greulich, and F. Clement, "Impact of boron doping profiles on the specific contact resistance of screen printed Ag–Al contacts on silicon," *Solar Energy Materials and Solar Cells*, vol. 142, pp. 2–11, 2015.

[3] N. Wöhrle, E. Lohmüller, J. Greulich, S. Werner, and S. Mack, "Towards Understanding the Characteristics of Ag-Al Spiking on Boron-Doped Silicon for Solar Cells," *Prog. Photovolt: Res. Appl,* submitted Sep. 2015.

[4] G. Schubert, "Thick film metallisation of crystalline silicon solar cells," Dissertation, Konstanz, Universität, Konstanz, 2006.

[5] R. Hoenig, "Evaluation and microstructure analysis of thick film contacts for industrial silicon solar cells," Dissertation, IMTEK, Albert-Ludwigs-University, 2014.

[6] S. M. Sze, *Physics of Semiconductor Devices*: Wiley, 1981/2007.

[7] A. Yu, "Electron tunneling and contact resistance of metal-silicon contact barriers," *Solid-State Electronics*, vol. 13, no. 2, pp. 239–247, 1970.

[8] R. A. Sinton, A. Cuevas, and M. Stuckings, "Quasi-steady-state photoconductance, a new method for solar cell material and device characterization," in *25th IEEE Photovoltaic Specialists Conference Washington DC: 1996*, 1996, pp. 457–460.

[9] D. E. Kane and R. M. Swanson, "Measurement of the emitter saturation current by a contactless photoconductivity decay method (silicon solar cells)," in *18th IEEE Photovoltaic Specialists Conference Las Vegas: 1985*, 1985, pp. 578–583.

[10] A. Kimmerle, P. Rothhardt, A. Wolf, and R. A. Sinton, "Increased Reliability for J0-analysis by QSSPC," *Energy Procedia*, vol. 55, pp. 101–106, 2014.

[11] Synopsys, "Sentaurus Device User Guide," vol. H-2013.03.

[12] R. A. Sinton and A. Cuevas, "A Quasi-Steady-State Open-Circuit Voltage Method for Solar Cell Characterization," in *16th EUPVSEC Glasgow*, 2000.

[13] A. S. Grove, O. Leistiko, and C. T. Sah, "Redistribution of Acceptor and Donor Impurities during Thermal Oxidation of Silicon," *J. Appl. Phys,* vol. 35, no. 9, p. 2695, 1964.
[14] K. Taniguchi, "Oxidation Enhanced Diffusion of Boron and Phosphorus in (100) Silicon," *J. Electrochem. Soc,* vol. 127, no. 10, p. 2243, 1980.
[15] H. Murrmann and D. Widmann, "Current crowding on metal contacts to planar devices," *IEEE Trans. Electron Devices*, vol. 16, no. 12, pp. 1022–1024, 1969.
[16] H. H. Berger, "Contact Resistance and Contact Resistivity," *J. Electrochem. Soc,* vol. 119, no. 4, p. 507, 1972.
[17] S. Kontermann, A. Ruf, R. Preu, and G. Willeke, "Simulating the interface morphology of silver thick film contacts on n-type Si-(100) and Si-(111)," *Appl. Phys. Lett,* vol. 101, no. 12, p. 121907, 2012.
[18] R. Lago, L. Pérez, H. Kerp, I. Freire, I. Hoces, N. Azkona, F. Recart, and J. C. Jimeno, "Screen printing metallization of boron emitters," *Prog. Photovolt: Res. Appl,* vol. 18, no. 1, pp. 20–27, 2010.
[19] F. D. Heinz, M. Breitwieser, P. Gundel, M. König, M. Hörteis, W. Warta, and M. C. Schubert, "Microscopic origin of the aluminium assisted spiking effects in n-type silicon solar cells," *Solar Energy Materials and Solar Cells*, vol. 131, pp. 105–109, 2014.
[20] S. Fritz, M. Konig, S. Riegel, A. Herguth, M. Horteis, and G. Hahn, "Formation of Ag/Al Screen-Printing Contacts on B Emitters," *IEEE Journal of Photovoltaics*, vol. 5, no. 1, pp. 145–151, 2015.